Vortex distributions near surface steps observed by scanning SQUID microscopy

B. L. T. Plourde* and D. J. Van Harlingen
Department of Physics, University of Illinois at Urbana-Champaign, 1110 West Green Street, Urbana, Illinois 61801

N. Saha, R. Besseling, M. B. S. Hesselberth, and P. H. Kes
Kamerlingh Onnes Laboratorium, Leiden University, P.O. Box 9504, 2300 RA Leiden, The Netherlands
(Received 20 January 2002; published 20 August 2002)

We have used a scanning superconducting quantum interference device microscope to image individual vortices near lithographically patterned surface steps in weak-pinning superconducting thin films of amorphous MoGe. The field-cooled vortex distributions are strongly influenced by the surface steps, with an enhanced vortex density along the thin side of the steps and a wide vortex-free region along the thick side of the steps. The surface steps induce orientational order that persists for many intervortex spacings away from the steps. We study the effects of surface step pinning for different magnetic-field strengths and step heights by analyzing the intervortex spacing and computing vortex correlation functions. For certain sample configurations, we are able to apply a Lorentz force to the vortices and observe an asymmetric vortex response near the surface steps. We discuss the interaction between a vortex and a surface step and consider possible mechanisms for generating the vortex distributions which we observe upon field cooling.

DOI: 10.1103/PhysRevB.66.054529 PACS number(s): 74.60.Ge, 74.76.−w

Vortices experience a wide variety of interaction potentials in type-II superconductors. Various sources of vortex pinning can lead to enhanced critical current densities for high current applications[1] and reduced flux noise in thin-film superconducting devices.[2] At low magnetic fields, surface steps and thickness variations in thin films can provide a substantial vortex pinning potential. The effects of surface step pinning can be observed best by imaging individual vortices near regions of controlled thickness variations in thin superconducting films. An understanding of vortex interactions with surface steps could lead to increased pinning in thin-film superconducting devices, thus improving performance. The use of lithographically patterned surface steps to control vortex distributions could be useful for studies of weak-pinning vortex channels[3] and in the realization of vortex ratchets.[4] At the mesoscopic level, vortex motion controlled by surface steps could make possible observations of quantum interference effects.[5]

A surface step can affect the vortex distribution and dynamics in several ways. The change in sample thickness across the step leads to a variation in the vortex line energy as determined by the line tension, $\epsilon_L \approx (\Phi_0/4\pi\lambda)^2 \ln\kappa$. This energy can be quite large, on the order of 100–1000 K nm of step height. In addition to the line energy change, the thickness variation near a step in a thin film can distort the distribution of vortex screening currents. In a superconducting film which is much thicker than the penetration depth, vortices oriented along the thin axis of the film can tilt to accommodate features such as surface steps. However, the samples presented in this paper were all fabricated from films which were thinner than the penetration depth, thus the vortices behave essentially as two-dimensional (2D) objects. Some of the first experimental studies of vortex interactions with steps involved transport measurements of superconducting films with periodic thickness variations.[6,7] More recently, direct magnetic imaging investigations of vortices in superconductors with surface steps have shown the influence of steps on the vortex distributions and dynamics.[8–14] Various magnetic imaging techniques are available for studying these distributions, including Bitter decoration,[15] Lorentz microscopy,[11] scanning Hall-probe microscopy,[16] magnetic force microscopy,[17] and magneto-optical imaging.[18] For low magnetic fields, scanning superconducting quantum interference device (SQUID) microscopy (SSM) provides the best resolution of individual vortices.[19,20]

We have observed substantial distortions of field-cooled vortex distributions in thin amorphous MoGe superconducting films with macroscopic etched surface trenches imaged with a SSM. Our SSM allows direct observation of the spatial distribution of vortices in the sample as a function of the cooling field strength for $B \leqslant 100$ mG. In the uniform region of the film far away from any trenches, as well as in samples with no trenches, we find a disordered vortex distribution with the average vortex density B/Φ_0 expected for cooling in a uniform magnetic-flux density, B, where we assume $B = H_a$ over most of the square during the cooling process, appropriate for this platelet geometry in a perpendicular field. However, inside the trench regions, we find that the average density of vortices is up to 50% higher than the density in the thick part of the sample. For a given value of B, the average vortex density in the trench is independent of the depth of the trench, at least for trench depths ranging from 25 nm to 125 nm on a 200-nm-thick film. The vortices in a trench are not evenly distributed, but rather form rows of enhanced vortex density along the thin side of the surface steps at the edges of the trench. In addition, we observe a vortex-free band in the thick region adjacent to the step before the vortex distribution recovers a uniform intervortex spacing further away from the trench. The trench edges induce orientational order in the vortex distributions both inside and outside the trench that persists for several lattice spacings.

Our SSM scans a 10-μm-diameter Nb pickup loop a few microns above the sample surface. The flux which penetrates

the pickup loop is coupled into a remote dc SQUID through a superconducting flux transformer. The SQUID is a custom Nb-trilayer device which we fabricate in our cleanroom facilities. An image is produced by raster scanning the pickup loop and SQUID over the sample surface at the end of a pivoted scan arm driven by room-temperature stepper motors. The SQUID and pickup loop assembly is attached to the scan arm with a flexible hinge that maintains it at a shallow angle with the sample while the tip of the pickup loop substrate is in contact with the sample surface. This allows the pickup loop to track the sample surface during scanning, maintaining a separation of a few microns, thus providing good spatial resolution. While the contact force between the tip and the sample is relatively weak, we find it advantageous to coat the sample with a protective insulation layer to prevent damage to the sample surface. We typically coat our samples with about 0.5 μm of sputtered SiO_2 and 0.1 μm of Al_2O_3. The entire SQUID assembly and sample are enclosed in a vacuum can which is immersed in a helium bath. The sample can be heated above the bath temperature with a noninductively wound heater. The bath is surrounded by a double-walled μ-metal shield which reduces the residual magnetic-flux density to less than 1 mG. This value was determined by cooling a superconducting film, then counting the number of vortices which are trapped in the film over a given area due to any residual field. A Helmholtz coil surrounding the sample allows for the application of small magnetic fields. For the images shown here, the applied magnetic field was held constant during the imaging. The size of the pickup loop determines the spatial resolution of the imaging. We are unable to resolve neighboring vortices if the spacing approaches the pickup loop diameter, 10 μm, thus we have primarily imaged these samples in small fields, below 100 mOe.

In weak-pinning superconductors, we have observed an interaction between the raster scanning and the vortices in the sample. This interaction causes shifts in the positions of vortices in the images, so that two repeated scans over the same area of a weak-pinning sample will yield different distributions of vortices. We have not observed these disturbances in previous images of stronger-pinning Nb films, placing a rough upper bound on the strength of the perturbing interaction. By studying the shifts of the vortex positions, we have determined that the interaction is localized to within a few microns of the contact point between the tip and the sample surface. The pickup loop is roughly 50 μm from this contact point. If we reverse the scan direction, such that the pickup loop images a vortex before it is passed over by the tip, then we obtain well-ordered vortex images, although a second scan over this same region would show significant shifts in the vortex positions. The reverse scan images obtained initially after field cooling appear to be unaffected by the interaction of the scanning tip with the vortices roughly 50 μm away from the image location, as no anisotropy related to the raster scan direction is observed in the orientational order of the resulting vortex distributions. The interaction between the vortices and the scanning tip, and possible applications of the controlled moving of vortices, will be discussed further in a future paper. All images in this paper were obtained with the reverse scan direction. This limits our imaging to a single pass over a particular region, following which the sample must be heated above T_c and then recooled in order to restore the intrinsic vortex order. Images upon recooling a given region in the same magnetic field yielded qualitatively similar vortex distributions.

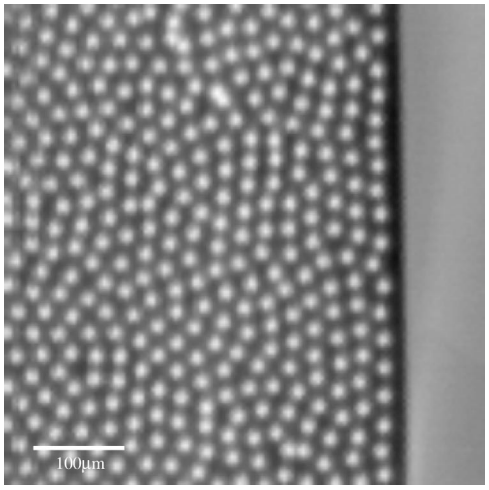

FIG. 1. Vortex distribution in a 200-nm-thick weak-pinning *a*-MoGe square with no surface steps. The sample was cooled in 30 mOe and the edge of the square is visible at the right side of the image.

The pinning properties of transition-metal glasses have been studied thoroughly,[21] and the weak bulk pinning ensures that the surface steps play a dominant role in the vortex potential landscape. Thin films of 200-nm-thick amorphous MoGe were sputter deposited onto Si substrates. The films had the following properties: $T_c = 6.5$ K, $\rho_n = 1.8$ $\mu\Omega$ m, and $S = dB_{c2}/dT|_{T_c} = -2.8$ T/K. Because of the short electronic mean free path in these films, the dirty-limit expressions can be applied, yielding $\lambda(0) = 550$ nm, $\xi(0) = 4.2$ nm, and $\kappa = 80$. The penetration depth at 4.2 K, where the images presented here were obtained, is about 670 nm, as measured with a two-coil screening technique. The films were patterned into a series of 2-mm-wide squares with standard photolithography and Ar-ion milling. Figure 1 contains a $(508\ \mu\text{m})^2$ image of the vortex distribution near the edge of one of these squares, cooled in 30 mOe. Even at this small magnetic field, the vortex pattern exhibits many regions of sixfold orientational order, although there is no long-range order. Except near the edge, the vortex density corresponds to $B \approx 30$ mG, confirming that $B = H_a$ for most of the sample, as expected for this geometry. There are no vortices within approximately one vortex spacing of the sample edge, as the screening currents are at a maximum here.

Surface trenches were generated by partially ion milling the squares in the pattern shown in Fig. 2(a). Each square contains only one depth of trench, which is in the range of 11 nm to 125 nm. A typical sample consists of four squares, spaced by several hundred microns, with a different trench depth in each square so that the sample as a whole covers the range of trench depths. The thickness variation near a trench

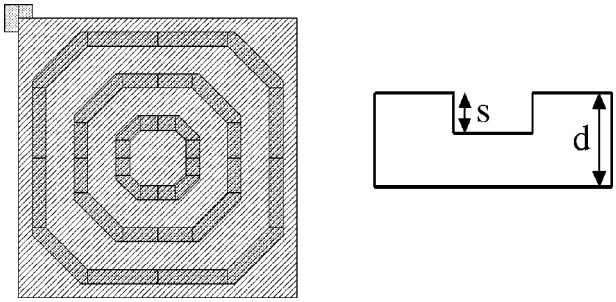

FIG. 2. Layout of sample with trench patterns. The three 100-μm-wide octagonal trenches were etched into the surface after the square was defined. Up to four different squares with different trench depths could be located on one sample.

is shown schematically in the cross section of Fig. 2(b). The typical field-cooled vortex distribution in the vicinity of a surface trench is shown in Fig. 3. The trench runs vertically in the center of the image, following the octagonal path. The average vortex density in the trench is higher than in the thick regions away from the trench, with excess vortices concentrated into two rows along the inside edges of each trench. Although the trench edges are not visible directly in the images, the separation of these two vortex rows is always several microns less than the trench width, confirming that the vortices are indeed pinned at the thin inside edge of the steps. In the thick region of the sample, there is a vortex-free region adjacent to each of the steps with a width on the order of the intervortex spacing. Beyond this vortex-free area, the vortices tend to form rows which are parallel to the trenches, indicating a long-range influence of the step pinning. Qualitatively similar vortex distributions around surface steps in other superconducting samples were observed with various magnetic imaging techniques, including Bitter decoration[8,10,13] and Lorentz microscopy.[11]

In order to quantify the influence of the surface steps on the vortex distributions, we have studied the effects of varying the magnetic-field strength and the surface step height with images around select locations of the *a*-MoGe squares. The vortex distribution in the vicinity of the trench can be described by four quantities: the width of the vortex-free region adjacent to the step, the vortex spacing in the high-density region along the surface steps, the average vortex density in the trench, and the vortex density in the thick region away from the trench. In addition, several image analysis techniques can be used to study the ordering of the vortex distributions around the trenches.

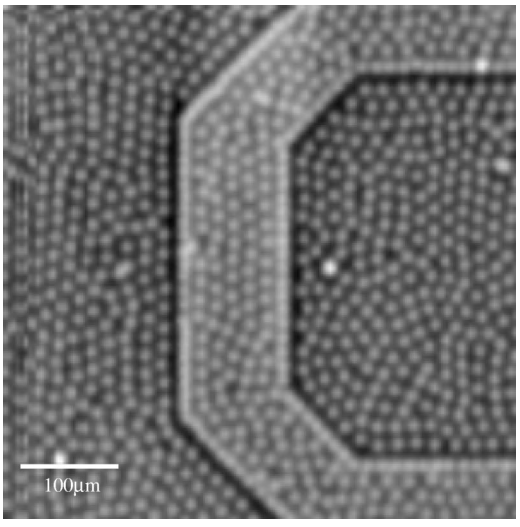

FIG. 3. Vortex distribution around the central 60-nm-deep octagonal trench in a 200-nm-thick *a*-MoGe square, cooled in 65 mOe.

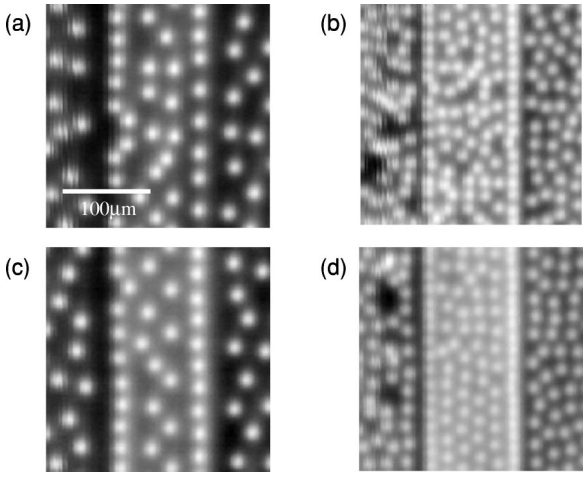

FIG. 4. Images around the central trench for different trench depths and cooling field strengths: (a) 25-nm steps, 16 mOe; (b) 25-nm steps, 48 mOe; (c) 125-nm steps, 16 mOe; and (d) 125-nm steps, 48 mOe.

Figure 4 contains four images obtained around the same region of the middle trench for the *a*-MoGe squares with 25-nm and 125-nm-deep trenches for two different cooling field strengths. As the sample is cooled in larger magnetic fields, both the vortex density along the steps and the overall vortex density increase. The width of the vortex-free region adjacent to the thick side of the steps decreases for larger fields. The vortices in the sample with the 125-nm-deep trench appear to be more strongly aligned with the steps and a larger fraction of the vortices in the trench are pinned at the step than those in the 25-nm-deep trench sample.

The width of the vortex-free regions in the thick portion of the square adjacent to the step can be estimated by measuring the distance between the high-density vortex row inside the trench and the vortices adjacent to the vortex-free region. In order to account for irregularities in the edge of the vortex-free region, this distance was measured at several different locations for each step, and the values were averaged. If the square contained a uniform triangular vortex lattice only, then the spacing between the row of vortices along the low side of the step and the first row of vortices parallel to the step on the thick side should be $b_0=(\sqrt{3}/2)a_0$, where $a_0=1.075\sqrt{\Phi_0/B}$ for a triangular lattice. Thus, we plot the widths of the vortex-free regions vs $B^{-1/2}$ in Fig. 5(a) for the four different trench depths. The data generally fall along a straight line which is about 20% steeper than the field dependence of the vortex row spacing in a uniform triangular lattice. Plotting the slopes of these linear fits for each step in

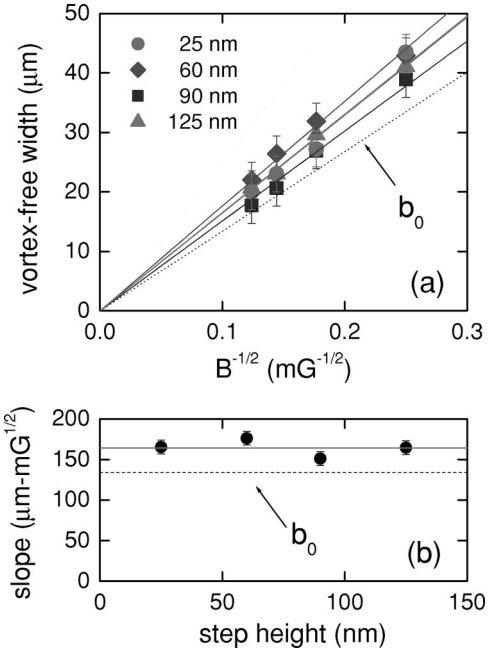

FIG. 5. Plot of the width of the vortex-free regions adjacent to the surface steps. (a) Width plotted against $B^{-1/2}$ for the four different trench depths along the step closer to the edge of the square, along with fits for each step height. The dashed line represents the vortex row spacing, b_0 for a uniform triangular lattice. (b) Plot of the slopes from the fits in (a) showing an independence of trench depth, where the dotted line is the corresponding value for b_0.

Fig. 5(b), we see that the widths of the vortex-free regions are essentially independent of the step height, over the range of trench depths imaged.

The vortex spacing in the high-density row along the low side of the surface step can be obtained directly from the image by counting the number of vortices in the row along a given length. We compare this measured vortex spacing, L, with the intervortex spacing expected for a uniform vortex lattice at the same field, a_0, by plotting $(1/L-1/a_0)/(1/a_0)$, the fractional enhancement of the vortex line density, as a function of the trench depth in Fig. 6. This graph shows that the vortex density along the steps is enhanced when compared with the uniform lattice with a compression which is larger for deeper trenches.

The average vortex density inside the trench can be determined by counting the number of vortices between the vortex-free regions along each step and dividing by the trench area in the image. The vortex density obtained in this manner is significantly higher than the density expected for a uniform vortex lattice with the corresponding value of vortex density, $n=B/\Phi_0$, and is essentially independent of the step height. This behavior can be seen in Fig. 7, where the average vortex density in the trench for the different step heights is plotted against the cooling flux density, B. For a given value of B, the data for the different step heights vary by no more than 3%. The plot also contains a straight line indicating the expected number of vortices for a uniform lattice in the trench, given by B/Φ_0. The total number of vortices in the trench is up to 60% larger than that expected for a uniform lattice. This enhancement is due predominantly to the

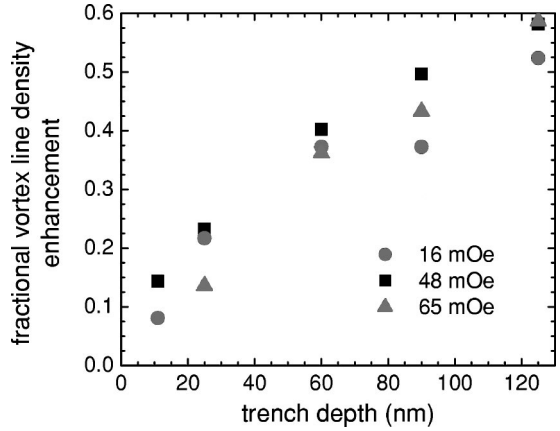

FIG. 6. Plot of the fractional enhancement of the vortex line density in the row along the low side of the steps for the *a*-MoGe squares. $(1/L-1/a_0)/(1/a_0)$ is plotted against the trench depth for several cooling field strengths, showing the compression of the vortices compared with the corresponding uniform lattice.

high-density vortex rows, although the vortex density between the rows is also about 10%–15% higher than B/Φ_0. The excess vortex density in between the rows is somewhat larger in shallower trenches, but this is offset by the greater compression of vortices in the high-density rows along the steps in the deeper trenches, shown in Fig. 6. Thus the total vortex density enhancement in the trenches is independent of the trench depth, as can be seen in Fig. 7. In contrast, the vortex density in the thick region of the square, away from the trenches, is not significantly altered. It can be estimated by counting the number of vortices in a given area directly. This average vortex density away from the trenches is also plotted in Fig. 7 for several of the different *a*-MoGe square samples presented in previous images, and the data fall within 5% of the uniform vortex lattice dependence, indicated by the dashed straight line.

A standard approach used to characterize ordering in vortex lattice images is the Delaunay triangulation technique. In this procedure, each vortex site is connected to its nearest

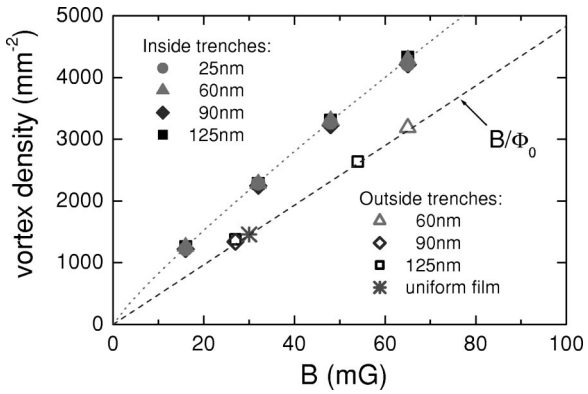

FIG. 7. Plot of average vortex density versus B for several different trench depths. The plot contains the average vortex density both in the trench regions and in the thick, uniform regions away from the trenches. Dashed line corresponds to the vortex density for a uniform lattice, B/Φ_0. Dotted curve is a guide to the eye.

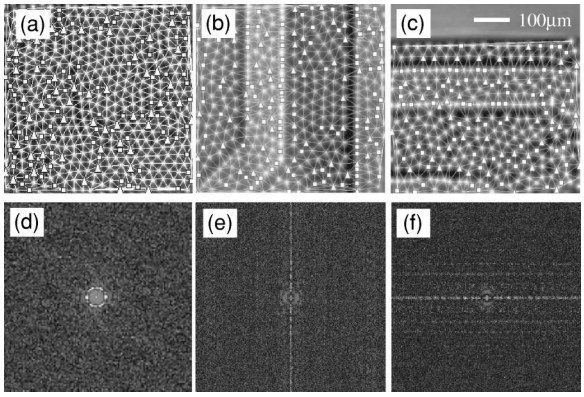

FIG. 8. Images around (a) the uniform sample and samples with trenches with different orientations, (b) the trench depth = 125 nm, running vertically, and (c) the trench depth = 90 nm, horizontally oriented. The images contain the Delaunay triangulations which join the vortex locations. Points with square symbols have a fivefold coordination and points with triangle symbols have a sevenfold coordination. The few sites with eightfold coordination are not marked. Image (a) is cooled in 32 mOe, and images (b) and (c) are obtained with a cooling field strength of 27 mOe. The corresponding autocorrelation functions are shown below each image in (d)–(f).

neighbors via bonds. To each lattice site, we can then assign a coordination number, n_i, equal to the number of nearest-neighbor bonds. The sites with coordination numbers other than six, characteristic of an Abrikosov triangular vortex lattice, are marked in the images to identify the location of defects in the lattice. Figures 8(a)–8(c) contain these triangulations for images of two samples with trenches and one with no trenches. Dislocation pairs of adjacent fivefold and sevenfold coordinated sites tend to form along the steps of the trenches due to the abrupt jump in vortex density across the step. Thus these defects along the steps are caused by the presence of the steps and are not necessarily related to intervortex interactions.

We can quantify the alignment of the vortex lattice induced by the trench edges in several ways. One approach is to calculate the vortex density autocorrelation function

$$G(\vec{r}) = \langle \rho(\vec{R})\rho(\vec{R}+\vec{r})\rangle_{\vec{R}}, \tag{1}$$

where $\rho(\vec{r})$ is the vortex density and the average is over the entire vortex distribution. This quantity gives the probability of finding another vortex at position $\vec{r}$ relative to any vortex lattice point. It can be calculated from a vortex image by identifying the position of each vortex, from which the vortex density function can be defined

$$\rho(\vec{r}) = \sum_i \delta(\vec{r}-\vec{r}_i). \tag{2}$$

The 2D Fourier transform of the density

$$F(\vec{k}) = \int \rho(r) e^{-i\vec{k}\cdot\vec{r}} d\vec{r} \tag{3}$$

is used to generate the vortex lattice structure factor,

$$S(\vec{k}) = \frac{F(\vec{k})F(\overrightarrow{-k})}{N_V}, \tag{4}$$

where N_V is the number of vortices in the image. The autocorrelation function is the inverse Fourier transform of the structure factor

$$G(\vec{r}) = \rho \int S(\vec{k}) e^{i\vec{k}\cdot\vec{r}} d\vec{k}, \tag{5}$$

where $\rho = N_V/A$ is the average vortex density over the image area A which contains vortices. Thus $G(\vec{r})$ gives the probability of finding a second vortex at a given displacement $\vec{r}$ from any point in the 2D vortex distribution. For a perfect triangular lattice, $G(\vec{r})$ is itself a triangular lattice, whereas a random vortex distribution produces no structure in $G(\vec{r})$. Figures 8(d)–8(f) show this quantity calculated for two images in samples with trenches with different orientations and one image of a sample with no trenches. There is little structure in $G(\vec{r})$ for the uniform sample [Fig. 8(d)], while $G(\vec{r})$ for the samples with trenches cooled in similar fields shows lines which indicate the alignment of vortices in rows parallel to the trench edges. The sample edge which is present in Fig. 8(c) does not influence the autocorrelation function, Fig. 8(f), as strongly as the trench. Autocorrelation functions calculated from images containing an edge of samples without trenches showed only weak structure related to the ordering relative to the sample edge. For samples containing trenches, the alignment along the trench orientation has a long range correlation of several vortex spacings along the direction parallel to the trenches. This is quite remarkable because at such low fields, the vortices are in a single vortex pinning regime where the intervortex interaction decays exponentially, thus closest neighbors interact only weakly. However, in the presence of surface steps there is a screening current flowing parallel to the trenches and this screening current interacts with the vortices to align them parallel to the trenches.

Another technique for characterizing the vortex distribution is to study the orientational order. Using the Delaunay triangulations, for each vortex *i*, we can assign each connecting bond $\vec{r}_{ij}$ an angle θ_{ij} measured relative to a fixed axis. From these, we define the orientational order parameter for each lattice site

$$\Psi_6(\vec{r}_i) = \frac{1}{n_i}\sum_{j=1}^{n_i} e^{i6\theta_{ij}}, \tag{6}$$

where the sum is taken over all n_i nearest-neighbor bonds of the point $\vec{r}_i$. A measure of the bond-orientational order of the lattice, based on this quantity, is the orientational correlation function, defined as

$$C_6(r) = \frac{1}{N(r)}\langle \Psi_6(\vec{R})\Psi_6^*(\vec{R}+\vec{r})\rangle_{\vec{R}}, \tag{7}$$

where the average is over the image and $N(r)$ is the number of pairs in the pattern separated by distance r. For a perfect triangular lattice, $C_6(r)$ should have peaks of unit height

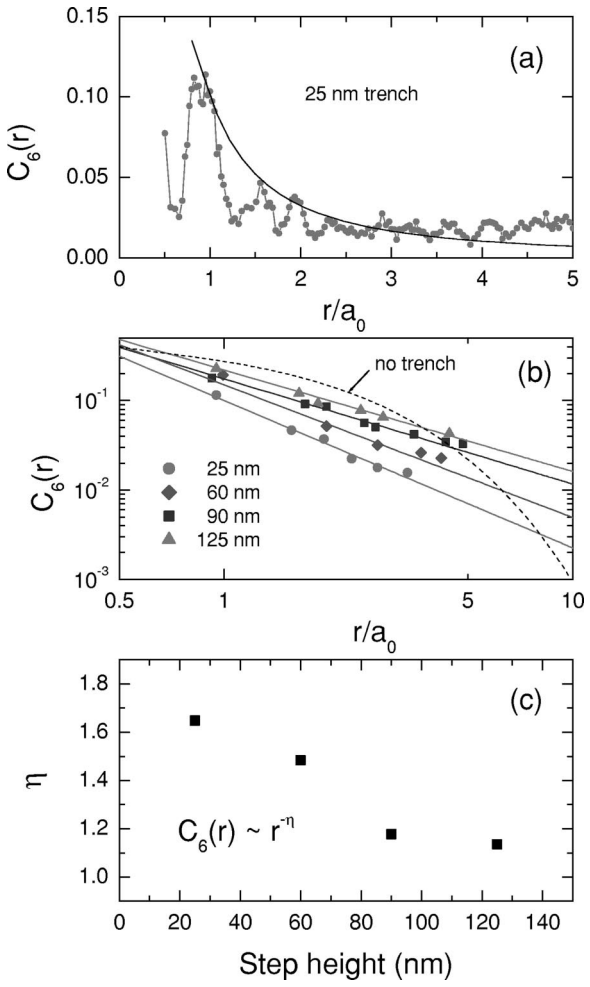

FIG. 9. (a) Plot of the orientational correlation functions as a function of average intervortex distance calculated from images of the sample with 25-nm-deep trenches, cooled in 27 mOe. The curve is a power-law fit. (b) Plots of peak heights of $C_6(r)$ for the four different trench depths, all cooled in 27 mOe, plotted on a log scale. The straight lines indicate power-law decay fits which are less steep for deeper trenches. Also shown is the exponential decay fit to the peak heights for a sample with no trenches cooled in 32 mOe. (c) Plot of decay exponents from the power-law fits versus depth of trench.

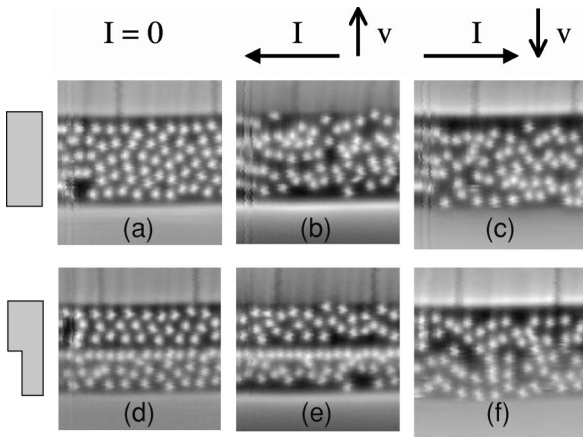

FIG. 10. Images of vortex shifting in 150-μm-wide, 100-nm-thick *a*-MoGe strips with and without a surface step. The corresponding strip cross section is shown to the left of each row of images. Transport current orientation and direction of vortex shift are indicated above images. (a) Strip with no step cooled in 43 mOe, and no applied transport current. (b) Strip with no step cooled in 43 mOe, then transport current increased to $+0.35$ mA ($\approx 2 \times 10^3$ A/cm^2), shifting the vortices towards the top edge of the strip. (c) Strip with no step cooled in 43 mOe, and transport current increased to -0.35 mA, shifting the vortices towards the bottom edge of the strip. (d) Strip with a 40-nm step cooled in 43 mOe, and no applied transport current. (e) Strip with a 40-nm step cooled in 43 mOe, then transport current increased to $+0.25$ mA ($\approx 2 \times 10^3$ A/cm^2), shifting the vortices towards the top edge of the strip, i.e., against the step. (f) Strip with a 40-nm step cooled in 43 mOe, and transport current increased to -0.25 mA, shifting the vortices towards the bottom edge of the strip, i.e., away from the step.

when r corresponds to a multiple of the lattice spacing. If the vortex distribution is amorphous, then $C_6(r)$ will decay exponentially, while if the vortex lattice has hexatic order only, it is expected that there is a power-law decay of $C_6(r)$.[22,23] Figure 9(a) shows $C_6(r)$ with r scaled by the average intervortex distance for the 25-nm-deep trench sample along with a power-law fit of the peak positions. The peak decays for this trenched sample and samples with three other trench depths are plotted on a log scale in Fig. 9(b), showing the power-law decays. For comparison, the peak decay for a sample without trenches is plotted, showing an exponential falloff. At small r, the magnitude of $C_6(r)$ for the samples with trenches is lower than that for the sample without trenches because $C_6(r)$ is calculated over the entire image, thus averaging over many defects which occur along the steps. The slopes of the plots of $\log_{10}[C_6(r)]$ vs intervortex spacing give the decay exponents which are plotted in Fig. 9(c), showing that for increasing step height, the decay exponent decreases. Thus the images of samples with trenches show more long-range orientational order than samples without trenches cooled in similar fields. Deeper trenches result in stronger orientational correlations.

In addition to observing field-cooled vortex patterns around surface trenches, we have imaged samples with a strip geometry, allowing us to drive transport currents through the vortex distribution. The strips were patterned with the same procedure used to produce the square samples described earlier. In the weak-pinning *a*-MoGe strips, small transport currents easily shift the vortex distribution across the strip width. Figure 10(a) contains an image of the field-cooled distribution in a 150-μm-wide *a*-MoGe strip with no surface step and no transport current. In Fig. 10(b), the transport current was increased to $+0.35$ mA ($j \approx 2 \times 10^3$ A/cm^2), with a corresponding Lorentz force towards the top of the image. The vortices are observed to shift towards the top of the image, and the self-field of the transport current can be seen as a brighter contrast of the bottom edge of the strip relative to the top edge. Figure 10(c) shows the shift of the vortex distribution towards the bottom edge of the strip for the opposite polarity of transport current.

The addition of a surface step to the strip makes the vortex response asymmetric. Figure 10(d) shows the field-

cooled vortex distribution in a 150-μm-wide, 100-nm-thick *a*-MoGe strip with a 40-nm surface step and no transport current. This image shows the typical vortex distribution, with a higher density of vortices along the low side of the step and relatively few vortices on the thick side adjacent to the step. As the transport current is increased with the Lorentz force directed against the step, the vortices are compressed into the step, but they do not cross from the thin side of the strip to the thick side, as shown in Fig. 10(e). Thus the vortex line tension barrier at the step impedes vortex motion up the step. For the opposite current polarity, with the Lorentz force directed away from the step, the vortices depin from the step and move towards the bottom edge of the strip, as shown in Fig. 10(f). At larger values of applied transport current, the images are complicated by the entry of new vortices into the strip due to the self-field of the transport current at the edges of the strip.

The vortex distributions and dynamics in patterned weak-pinning films are influenced dramatically by the presence of etched surface steps. The images of field-cooled vortices near trenches show an enhanced density of vortices pinned along the thin side of the steps and a vortex-free region in the thick portions of the film adjacent to the steps. As noted previously, these distributions are qualitatively similar to those obtained in other vortex imaging studies around naturally occurring surface steps in various superconductors using several different techniques.[8,11–13] As a result, we do not believe that the vortex distributions we observe are related to possible damage due to the ion-milling process. This was tested directly by fabricating an *a*-MoGe square sample in which the entire surface of the square was partially ion milled prior to patterning the trenches. After etching the square shape into the film as described above, the entire surface of the 200-nm-thick square was ion milled down to a thickness of 150 nm. Octagonal trenches were then patterned and ion milled further to a depth of 43 nm. SSM images in the vicinity of the trench displayed the same excess concentration of vortices along the low side of the steps and same vortex-free region adjacent to the step. Thus if the milling caused any surface damage in the thick region away from the trench, it did not noticeably affect the observed vortex distributions.

The distribution of vortices in the vicinity of the trench edges is likely determined by several factors. One significant contribution is the substantial vortex line energy barrier at the steps. For our *a*-MoGe films, this energy ranges between 4.8×10^3 K and 2.4×10^4 K for the step heights we have fabricated. This barrier prevents the motion of vortices from thin to thick regions across a step. Thus the motion of vortices across a transverse step driven by transport currents is asymmetric. This dynamical mechanism was invoked to explain a similar response observed in Bitter decoration images of vortex creep near surface steps in $NbSe_2$ crystals.[9] In our experiments, vortices which nucleate in the trenches during the field cooling are inhibited from escaping out of the trench by the line energy barrier.[12] Larger jumps in line energy, corresponding to taller steps, pin vortices more strongly, as shown by the plot of vortex density along the low side of the steps in Fig. 6. Also the taller steps lead to a stronger ordering of the vortex distribution parallel to the step directions.

However, we do not believe that the line energy effect is by itself sufficient to explain our images. In the first place, we observe the vortex distortion near the step even in samples cooled and imaged in the applied magnetic field. In this case, there should not be forces trying to expel the vortices from the samples, eliminating any dynamical mechanism as the origin of the vortex distributions. Also, the enhanced vortex density in the trenches and the width of the vortex-free regions which we observe are independent of trench depth. One would expect some variation with trench depth if the change in vortex line energy dominated the behavior. It is our view that it is necessary to consider the distortion of screening currents near the step edges and the possibility of surface superconductivity along the edges to develop a full model for the vortex distortion.

The abrupt change in vortex density at the edges of the trenches corresponds to substantial screening currents flowing along the steps. These screening currents repel vortices in the thick region away from the steps, producing the vortex-free regions. This phenomenon was previously analyzed by considering the screening current distributions around a circular hole in a superconducting film for different numbers of vortices trapped in the hole.[24] If a finite quantized flux is trapped in the hole, then the screening current associated with this flux is peaked near the perimeter of the hole. Thus a vortex outside of the hole will be pushed away due to the Lorentz force associated with the screening currents. If more flux is trapped in the cavity, then the current-density peak moves in closer to the perimeter of the cavity. Thus the width of the vortex-free region adjacent to the cavity should decrease for larger cooling magnetic-field strengths, as shown in the measured field dependence plotted in Fig. 5(a). This field dependence follows a similar trend to that expected for the spacing of the first vortex row from a sample edge based on magnetization screening currents flowing along the sample edge.[25–27] However, such a treatment does not agree quantitatively with the data of Fig. 5(a), as the calculation of Ref. 25 does not apply for flux densities less than $\Phi_0/(\lambda^2/d)^2\approx4$ G. A model accounting for the discrete vortex positions at the low fields of our images as well as the influence of the flux in the trench on the screening currents at the steps is required.

The pinning of the vortices at the inside edge of the trench is more difficult to explain. The distribution of the screening current around each vortex should be distorted near the surface steps. The related problem of a vortex near the interface of two superconductors with different penetration depths was first considered in Ref. 28. The authors calculated the formation of a vortex potential minimum located near the interface, leading to the pinning of a row of vortices along the interface. Such a mechanism could be applied to the *a*-MoGe square trench samples presented in this work, as the film thickness everywhere is less than the penetration depth of 670 nm. Thus the effective thin-film penetration depth, λ^2/d, is indeed different between the thin region in the trench and the thick regions in the rest of the square. However, direct application of this model to the surface step problem predicts

a row of vortices pinned along the thick side of the surface step, rather than the high vortex density we observe along the thin side. This may be because the variable penetration depth model does not account for the enhanced vortex density in the trenches which appears to arise during the field-cooling process nor for the screening currents along the edges. We note that we were unable to compare the field-cooled vortex distributions with images of vortices which enter the sample after ramping up the magnetic field from a zero-field-cooled state, as the entry fields were too large for the operation of the SSM.

A similar increase in vortex density in surface depressions was observed in Bitter decoration imaging experiments.[10] In this work, the authors imaged field-cooled vortex distributions around small ($\leqslant 2.2$ μm in radius) circular surface depressions in Nb films. The vortices were compressed into the thinner depressions up to a density which was considerably larger than that in the rest of the film away from the depressions. Also, the vortices were located primarily around the inside of the perimeter, i.e., at the low side of the surface steps. In addition, the observed compression was essentially independent of the depth of the depression. Bezryadin *et al.*[10] proposed that the increased vortex density in the depressions was caused by a surface superconducting state which developed along the face of the perimeter of the depressions. As the sample was cooled from above T_c in a magnetic field, the faces of the surface steps which are parallel to the field could become superconducting at a slightly higher temperature than the rest of the sample due to the surface superconductivity phenomenon. Thus there could be a narrow temperature interval below the temperature at which the faces of the steps become superconducting, $T(H_{c3})$, and above the T_c of the rest of the sample. The requirement of continuity of the surface superconducting order parameter around the perimeter of the depression would cause the compression of flux into the region, with a stepwise increase as more loops are added to the order parameter. As the temperature is lowered through T_c, the flux compression results in a higher vortex density in the depression. A theoretical treatment of this behavior indicated that the amount of flux compression would be independent of the height of the surface steps, as long as the step height remained finite.[10] Although this picture accounts for some of the qualitative features of our images, it is highly unlikely that a single continuous surface superconducting order parameter would exist along the face of the entire perimeter of each of the trenches in the square samples we have imaged, as this would cover a length on the order of 1 cm. Instead, any surface superconducting state would probably be broken into patches by defects along the length of the steps. Thus the flux could still be compressed into the trenches during the cooling process due to the distortion of the magnetic-field lines by the superconducting patches for temperatures between $T(H_{c3})$ and T_c. In the future, experiments are planned to test this theory by coating the samples with a blanket layer of a normal metal. The different boundary conditions at the superconductor/normal interface should prevent the formation of any surface superconducting state.

Careful counting of the vortices in our *a*-MoGe sample indicates that the substantial increase in the number of vortices in the trenches appears to outweigh the decrease in vortex density away from the trench regions and, in particular, the vortex-free areas adjacent to the steps. Such an enhancement of the vortex density is reminiscent of the paramagnetic Meissner effect (PME) observed in various superconductors cooled in small magnetic fields.[29,30] Studies of the PME in Nb disks have a strong dependence on surface damage.[31] Samples with clean surfaces exhibited a conventional diamagnetic response during field cooling, while disks with damaged surfaces developed a paramagnetic response. In order to investigate the possibility of a PME due to the surface steps in our samples, further imaging is needed, using smaller film patterns which fit within one SSM scan window, thus simplifying the vortex counting. Additionally, imaging experiments will be performed with samples containing different trench patterns, including trenches which cross the sample edge.

In summary, our studies of the vortex distributions in patterned weak-pinning thin films show a strong influence from surface steps. The images of clearly resolved vortices are made possible by the excellent flux sensitivity and good spatial resolution of the SSM. For low magnetic fields, the surface steps substantially distort the field-cooled vortex distributions. We have also observed the effects of the line energy barrier at a step in the asymmetric response of vortices near a step to an applied Lorentz force. Using the strong pinning of surface steps, it may be possible to control vortex distributions in thin films at the mesoscopic level with patterned trenches. The substantial vortex density enhancement we observe in the trenches may be related to the PME, although further measurements are required to confirm this.

We would like to thank Mark Wistrom and Kevin Osborn for key technical assistance. We have also benefited from theoretical discussions with Denis Vodolazov, John Clem, and Franco Nori. This research was supported by the National Science Foundation Grants No. DMR91-20000, DMR97-05695, and DMR01-07253. We acknowledge extensive use of the microfabrication facilities of the Frederick Seitz Materials Research Laboratory at the University of Illinois at Urbana-Champaign.

*Present address: Department of Physics, University of California, Berkeley, CA 94720.

[1] H. Ullmaier, *Irreversible Properties of Type II Superconductors* (Springer-Verlag, Berlin, 1975).

[2] D. Koelle, R. Kleiner, F. Ludwig, E. Dantsker, and J. Clarke, Rev. Mod. Phys. **71**, 631 (1999).

[3] A. Pruymboom, P.H. Kes, E. Van der Drift, and S. Radelaar, Phys. Rev. Lett. **60**, 1430 (1988).

[4] J.F. Wambaugh, C. Reichhardt, C.J. Olson, F. Marchesoni, and F. Nori, Phys. Rev. Lett. **83**, 5106 (1999).

[5] P. Ao and X.-M. Zhu, Phys. Rev. Lett. **74**, 4718 (1995).

[6] D.D. Morrison and R.M. Rose, Phys. Rev. Lett. **25**, 356 (1970).

[7] O. Daldini, P. Martinoli, J.L. Olsen, and G. Berner, Phys. Rev. Lett. **32**, 218 (1974).

[8] H. Dai, J. Liu, and C.M. Lieber, Phys. Rev. Lett. **72**, 748 (1994).
[9] F. Pardo, F. de la Cruz, P.L. Gammel, E. Bucher, C. Ogelsby, and D.J. Bishop, Phys. Rev. Lett. **79**, 1369 (1997).
[10] A. Bezryadin, Y.N. Ovchinnikov, and B. Pannetier, Phys. Rev. B **53**, 8553 (1996).
[11] K. Harada, H. Kasai, T. Matsuda, M. Yamasaki, J.E. Bonevich, and A. Tonomurai, Jpn. J. Appl. Phys., Part 1 **33**, 2534 (1994).
[12] B.L.T. Plourde and D.J. Van Harlingen, *Physics and Materials Science of Vortex States, Flux Pinning and Dynamics* (Kluwer Academic, Dordrecht, 1998), Vol. 356, p. 281.
[13] L.Y. Vinnikov, T.L. Barkov, B. Irmer, K. Kragler, and G. Saemann-Ischenko, Physica C **308**, 99 (1998).
[14] T. Schuster, M.R. Koblischka, H. Kuhn, H. Kronmüller, G. Friedl, B. Roas, and L. Schultz, Appl. Phys. Lett. **62**, 768 (1993).
[15] H. Träuble and U. Essmann, J. Appl. Phys. **39**, 4052 (1968).
[16] A. Oral, S.J. Bending, and M. Henini, Appl. Phys. Lett. **69**, 1324 (1996).
[17] A. Volodin, K. Ternst, C.V. Haesendonck, and Y. Bruynseraede, Appl. Phys. Lett. **73**, 1134 (1998).
[18] M.R. Koblischka and R.J. Wijngaarden, Supercond. Sci. Technol. **8**, 199 (1995).
[19] J.R. Kirtley and J.J.P. Wikswo, Annu. Rev. Mater. Sci. **29**, 117 (1999).
[20] L.N. Vu and D.J.V. Harlingen, IEEE Trans. Appl. Supercond. **3**, 1918 (1993).
[21] P.H. Kes and C.C. Tsuei, Phys. Rev. B **28**, 5126 (1983).
[22] B.I. Halperin and D.R. Nelson, Phys. Rev. Lett. **41**, 121 (1978).
[23] D.R. Nelson, M. Rubinstein, and F. Spaepen, Philos. Mag. A **46**, 105 (1982).
[24] G.S. Mkrtchyan and V.V. Shmidt, Zh. Éksp. Teor. Fiz. **61**, 367 (1971) [Sov. Phys. JETP **36**, 352 (1973)].
[25] A.E. Koshelev, Physica C **223**, 276 (1994).
[26] A.E. Koshelev, Phys. Rev. B **50**, 506 (1994).
[27] A.E. Koshelev, Phys. Rev. B **51**, 12 063 (1995).
[28] G.S. Mkrtchyan and V.V. Shmidt, Zh. Éksp. Teor. Fiz. **68**, 186 (1975) [Sov. Phys. JETP **34**, 195 (1972)].
[29] W. Braunisch, N. Knauf, V. Kataev, S. Neuhasen, A. Grutz, A. Kock, B. Roden, D. Khomskii, and D. Wohlleben, Phys. Rev. Lett. **68**, 1908 (1992).
[30] A.K. Geim, S.V. Dubonos, J.G.S. Lok, M. Henini, and J.C. Maan, Nature (London) **396**, 144 (1998).
[31] D.J. Thompson, L.E. Wenger, and J.T. Chen, Phys. Rev. B **54**, 16 096 (1996).